Liquid-to-glass transition in bulk glass-forming $Cu_{60}Ti_{20}Zr_{20}$ alloy by molecular dynamics simulations

X. J. Han* and H. Teichler†
Institut für Materialphysik, Universität Göttingen, D-37077 Göttingen, Germany
(Received 26 September 2006; published 11 June 2007)

We report results from molecular dynamics studies concerning the microscopic structure and dynamics of the ternary, bulk metallic glass-forming $Cu_{60}Ti_{20}Zr_{20}$ alloy. In detail we consider the partial radial distribution functions, nearest-neighbor numbers, specific heat, simulated glass temperature, diffusion coefficients, and incoherent intermediate scattering function (ISF). The applied atomic model reproduces well experimental x-ray data of the total radial distribution function. It provides for $Cu_{60}Ti_{20}Zr_{20}$ a structure with marked intermediate-range order. The ISF is analyzed within an extension of mode-coupling theory, where the effective memory kernel is evaluated from the Laplace transform of the ISF. The dynamics of the system fulfills in most respects the predictions of mode-coupling theory (MCT), up to an absence of the algebraic t^{-a} decay in the early β range. Comparison with the calculated memory kernel shows that this absence can be traced back to deviations of the kernel from its approximate form analyzed in MCT. As by-product, our investigation provides a method to reconstruct around the critical temperature major parts of the memory kernel from λ and the plateau value f^c of the ISF, and it indicates why the critical dynamics predicted by mode-coupling theory can be observed in a temperature interval of more than 500 K.

DOI: 10.1103/PhysRevE.75.061501 PACS number(s): 64.70.Pf, 61.20.Ja, 61.20.Lc

I. INTRODUCTION

With favorable mechanical behavior and good resistance to corrosion, multicomponent bulk metallic glasses (BMGs) have attracted extensive research interest [1–5] since the first synthesis of the La-Al-Ni BMG by copper mold casting in 1989 [1]. However, despite the great achievements in preparation and characterization of these materials, the specific details of the liquid-to-glass transition of multicomponent BMGs have not been fully understood yet and are still an open question. Here we present results of a molecular dynamics (MD) analysis of the BMG-forming $Cu_{60}Ti_{20}Zr_{20}$ ternary alloy. MD simulations have turned out to be a powerful tool for obtaining insight into the structure and dynamics of vitrifying melts on the atomic scale. For multicomponent metallic glass-forming systems, MD investigations are rather scarce (but see, e.g., [6–8]), while the method was successfully used to study aspects of the liquid-to-glass transition of binary amorphous metallic alloys (e.g., [9–13]), of the SiO_2 melt [14], glass-forming molecular systems [15,16], or chalcogenids [17]. In particular from the class of the multicomponent BMGs, so far only $Al_{15}Ni_{25}Zr_{60}$ has been studied by MD modeling, with the main emphasize on structural aspects [7].

There are two reasons for choosing $Cu_{60}Ti_{20}Zr_{20}$. First, $Cu_{60}Ti_{20}Zr_{20}$ is of technological interest. It belongs to the family of Cu-based BMGs which combine high strength with good ductility. Among the $Cu_{60}Zr_{40-x}Ti_x$ alloys, $Cu_{60}Ti_{20}Zr_{20}$ has the highest glass-forming ability, with a reduced glass transition temperature T_g/T_l of 0.63. Second, from a fundamental point of view, MD analysis of $Cu_{60}Ti_{20}Zr_{20}$ is of much interest, as this alloy exhibits rather different atomic interactions than the previously studied $Al_{15}Ni_{25}Zr_{60}$. While both systems are fully metallic, $Cu_{60}Ti_{20}Zr_{20}$ is an alloy with rather weak atomic pair interactions among the majority Cu species and strong effects of the electron gas, making that the Cu atoms act like flexible glue, whereas in $Al_{15}Ni_{25}Zr_{60}$ the atoms of the majority component, Zr, have the strongest, covalent atomic pair interaction of all its constituents and form a rather rigid matrix.

In our analysis of the MD-simulated dynamics of the $Cu_{60}Ti_{20}Zr_{20}$ melt we make use of basic results of mode coupling theory (MCT) [18–22], which is one of the most successful theoretical approaches to describe the liquid side of the liquid-to-glass transition. MCT provides detailed predictions on the time and temperature dependence of the fluctuation dynamics in the vitrifying melt, where only two parameters matter: There is the exponent parameter, which determines the nonuniversal critical exponents and comparable material coefficients of the melt, and the control parameter, which describes the distance of temperature—or any other quantity like the density—from the critical temperature and density, respectively. Many predictions of MCT have been verified qualitatively and quantitatively for a variety of materials—e.g., the Lennard-Jones fluid [23,24] and binary metallic alloys [10,11]. There is, however, one particular discrepancy between the MCT predictions and the data of MD simulations in the so-called early β regime of the intermediate scattering function. Already in the early investigation by Lewis and Wahnström [15] this discrepancy was ascribed to vibration-type particle motions not fully taken into account in MCT. However, a feasible proof of this explanation is lacking so far.

We here follow basic lines of MCT. But while MCT either uses for the memory kernel $F(t)$ a systematic low-order approximation [11,25–27] or—in its schematic version—a phenomenological expression [28], we here take up our recent

*Electronic address: x.han@fz-juelich.de
†Author to whom correspondence should be addressed. Electronic address: teichler@ump.gwdg.de

approach [10,11] and treat $F(t)$ as an unknown function, which is evaluated by Laplace transform from the intermediate scattering function $\Phi(t)$ and the related equation of motion, once $\Phi(t)$ is known, e.g., from MD simulations. This allows us to test which of the basic assumptions of MCT, especially of the schematic theory, are fulfilled in the analyzed system here. In this context we then shall make some remarks concerning the difficulties of MCT to describe the early β regime.

The organization of the present contribution is as follows: In the next section, Sec. II, we describe the model applied in our MD simulations and the methods used for analyzing the data, including a short description concerning our handling of the memory kernel. The results of our simulations are presented and discussed in Sec. III. Section IV then gives a summary of our findings and some concluding remarks.

II. MODEL AND METHODS

A. Molecular dynamics model

Molecular dynamics simulations are performed for a system containing 1372 atoms in an orthorhombic box with periodic boundary conditions in three directions. At constant temperature T and zero external pressure P, the equations of motion are integrated by a fifth-order predictor-corrector algorithm with a time step of 2.5×10^{-15} s. For maintaining constant temperature and constant pressure, a Berendsen thermostat and barostat [29] are used.

In order to describe the atomic interactions in the ternary Cu-Ti-Zr alloy, a microscopic model is applied similar to the one used in our previous work for the binary Ni-Zr [10,11] and the ternary Ni-Zr-Al alloys [7].

According to this model, the potential energy is composed of two parts:

$$E_{pot} = \sum_{i,j} \varphi(r_{ij}) + E_{vol}(V). \tag{1}$$

Here, $\varphi(r)$ is a short-range pair potential, which aims at taking care of electronic d-state interactions and residual local couplings between s and p states, and $E_{vol}(V)$ is a volume-dependent electron gas term.

The pair potentials take the form of Stillinger-Weber (SW) potentials,

$$\varphi(r) = A\left(\frac{1}{(\alpha r)^n} - 1\right)\exp\left(\frac{1}{\alpha r - a_1}\right), \quad 0 < r \leqslant r_{cut} = a_1/\alpha. \tag{2}$$

For the electron gas term, we use the expression of Finnis [30]:

$$E_{vol}(V) = NN_s\left(\frac{a}{r_s^2} - \frac{b}{r_s} + c\ln\frac{r_s}{r_B} - d\right), \tag{3}$$

with electron radius

$$r_s^3 = \frac{3V}{4N\pi N_s}. \tag{4}$$

N_s is the average number of s electrons,

TABLE I. Parameters for the electron gas term of the potential.

a (eV nm^2)	b (eV nm)	c (eV)	d (eV)	$N_{s,Cu}$	$N_{s,Ti}$	$N_{s,Zr}$
0.037332	0.51241	0.42172	1.4966	1.38	1.39	1.3

$$N_s = \sum_i x_i N_{s,i}, \tag{5}$$

N the number of simulated particles, V the volume of the system, r_B the Bohr radius, x_i the concentration of species i, and $N_{s,i}$ the effective number of s electrons for species i. The parameters a, b, c, d, and $N_{s,i}$ are listed in Table I.

For estimating the pair-potential parameters, information from the Hausleitner-Hafner hybridized nearly-free-electron tight-binding-bond model [31,32] and experimental data are combined. The fitting SW parameters of Cu-Zr-Ti are listed in Table II.

The Zr-Zr interaction is taken from [10,11] with parameter A rescaled to bring the simulated melting temperature closer to the experimental value. The parameters of the Ti-Ti interaction are selected to bring the values of simulated lattice constant, c/a ratio, and cohesion energy of the crystalline sample to a fair relation with the experimental data, assuming a short-range potential with cutoff radius $r_c = a_1/\alpha$ smaller than the next-nearest-neighbor distance in the crystal. The Cu-Cu interaction is constructed to provide acceptable values for the simulated lattice constant and cohesion energy, under the restriction to nearest-neighbor interactions. For the Cu-Ti and Zr-Ti interactions, the parameters are selected to present sufficiently well the lattice constants of $CuTi_2$, CuTi, $CuZr_2$, and CuZr. Finally, the Ti-Zr interaction parameters are chosen approximately halfway between the values for the pure components, taking into account the full miscibility in the Ti-Zr system and the nearly vanishing mixing enthalpy between the components.

Appendix A gives a comparison of the calculated and experimental data of some crystalline phases aimed at testing the present model.

As a further test, we determined the total radial distribution function of $Cu_{60}Ti_{20}Zr_{20}$ alloy in the glassy state of 300 K on the basis of this model. The simulation result is presented in Fig. 1, which also includes the experimental data of Mattern *et al.* from an x-ray diffraction [33]. The

TABLE II. SW potential parameters used in the simulation for $Cu_{60}Ti_{20}Zr_{20}$.

	A (eV)	α^{-1} (Å)	a_1	n
Cu-Cu	0.485	2.275	1.681	9
Cu-Ti	1.695	2.300	1.794	7
Ti-Ti	1.588	2.350	2.056	4
Cu-Zr	1.943	2.496	1.792	8
Ti-Zr	2.722	2.481	1.968	3
Zr-Zr	3.655	2.646	1.855	3

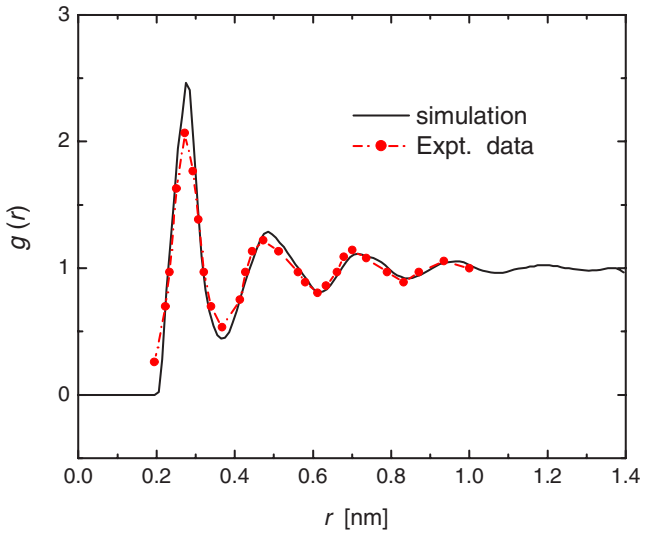

FIG. 1. (Color online) Total radial distribution function of experimental [33] and simulated amorphous $Cu_{60}Ti_{20}Zr_{20}$ at 300 K.

good agreement between simulation and experimental results indicates that our microscopic model is quite suitable to describe the atomic interaction of the Cu-Ti-Zr ternary alloy system. Regarding this, we should emphasize that the parameters of the simulation model have not been adapted to the experimental x-ray data.

In order to generate the ternary liquid structure, we start with hypothetic face-centered-cubic configuration, which is equilibrated at 1700 K for 5 ns, leading to a homogeneous liquid state. Then the system is cooled down to given temperatures with a cooling rate of 3×10^{10} K/s. The resulting configurations are relaxed by additional isothermal annealing runs, and then production runs are carried out and used for detailed data analysis at the selected temperature.

B. Analysis of dynamics: Self-diffusion coefficients, intermediate scattering function, and critical temperature of the mode-coupling theory

The self-diffusion coefficients D_A (A=Cu, Zr, Ti) are calculated according to

$$D_A = \lim_{t\to\infty} \frac{1}{6t} \langle\langle r^2(t)\rangle\rangle_A, \tag{6}$$

from the mean-square displacement (MSD)

$$\langle\langle r^2(t)\rangle\rangle_A = \langle\langle |x_n(\tau+t) - x_n(\tau)|^2\rangle\rangle_{n\in A}. \tag{7}$$

Here the double brackets mean averages over the particles n of type A and over the evolution time τ. The temperature dependence of the coefficients D_A is tested regarding the prediction of the MCT [34],

$$D_A(T) \sim |T - T_c|^\gamma \quad (T > T_c), \tag{8}$$

and regarding agreement with the Vogel-Fulcher-Tammann (VFT) law [35–37]

$$D_A(T) = D_A^0 \exp[-Q/(T - T_0)] \quad (T > T_0), \tag{9}$$

where the VFT temperature T_0 is assumed to have a value below T_g. T_c is the material specific critical temperature of MCT. It can be estimated from independent dynamical quantities, such as the intermediate scattering function (ISF) (e.g., [11,24]). As is indicated in the next paragraph, MCT predicts an intimate relationship between the value of γ and the parameters that govern the time evolution of the ISF.

The incoherent intermediate scattering function $\Phi_A(q,t)$ is evaluated from

$$\Phi_A(q,t) = \langle\langle \exp\{iq[x_n(\tau+t) - x_n(\tau)]\}\rangle\rangle_{n\in A}. \tag{10}$$

The double brackets again indicate averaging over all atoms of type A and the evolution time τ as described for the MSD.

In case of Hamiltonian dynamics for the particles, the Lanczos recursion scheme yields for Φ_A the exact evolution equation [11]

$$\Phi_A(t) + \Omega_A^{-2}\partial_t^2\Phi_A(t) + \int_0^t dt' F_A(t-t')\partial_t\Phi_A(t') = 0, \tag{11}$$

with $\Phi_A(t=0)=1$, $\partial_\tau\Phi_A(0)=0$, $\Omega_A^{-2}=q^2k_BT/m_A$, and the memory kernel F_A depending on q and T. While in binary and multicomponent systems the coherent ISFs are solutions of matricial equations (compare, e.g., [26,27,11]), the incoherent ISFs are solutions of scalar equations like Eq. (11), following from the Lanczos recursion scheme. The mathematics for solving Eq. (11) and detailed properties of the solutions have been developed in the context of the schematic MCT (e.g., [20,34]). Within the full MCT, explicit approximations have been deduced for F_A [25–27] in terms of coherent and incoherent ISFs, which turned out to be well applicable to describe essential features of the time and temperature dependence of the correlators Φ_A as well as of the temperature dependence, e.g., of the viscosity [29,34]. The theory predicts, in particular, the existence of nonvanishing asymptotic values

$$\Phi_A(q, t\to\infty) = f_A^c(q) > 0 \tag{12}$$

for temperatures below a critical T_c, which means the existence of an arrested state with nondecaying structural correlations.

In our analysis we adopt from the schematic MCT [18,19,28] detailed results about solutions of equations like Eq. (11). In the schematic MCT, one restricts oneself to one relevant correlator Φ_A with properly selected q, and F_A is modeled by a polynomial in Φ_A, e.g., $F_{rs,A}=\lambda_1\Phi_A^r+\lambda_2\Phi_A^s$, plus a singular contribution $\eta\delta(\tau^+)$. λ_1 and λ_2 are functions of temperature and/or of density of the system. Within this approach, T_c is the highest temperature at which the relation

$$f_A^c/(1-f_A^c) = F_{rs,A}(f_A^c) \tag{13}$$

is fulfilled, with f_A^c defined by Eq. (12).

According to MCT, around T_c the correlator Φ_A shows, on a logarithmic time scale, an initial decay due to particle vibrations, a broad shoulder, the so-called β regime, and—above T_c—the final α decay. In detail, around T_c the correlator Φ_A behaves like

$$\Phi_A(t) = f_A^c + h(t), \tag{14}$$

$$h(t) = A/t^a, \quad t < t_\varepsilon, \tag{15}$$

and

$$h(t) = \text{const}, \quad \text{for } t_\varepsilon < t \text{ and } T < T_c, \tag{16}$$

$$h(t) = -Bt^b, \quad \text{for } t_\varepsilon < t \ll \tau_\alpha \text{ and } T > T_c. \tag{17}$$

Here t_ε sets the time scale of the β-relaxation regime and τ_α means the relaxation time of the final α decay.

For the late α-relaxation regime the correlation function can be well approximated by the Kohlrausch-Williams-Watts (KWW) function

$$\Phi(q,t) = A_0 \exp[-(t/\tau_\alpha)^\beta]. \tag{18}$$

It has been shown [38] that Eq. (18) becomes an exact solution in simple liquids in the case of large values of q.

It is one of the great achievements of the MCT that it traces back all the exponents in Eqs. (14)–(18) to one "exponent parameter" λ, which is related to the memory kernel F_A by [28]

$$\lambda = \tfrac{1}{2}\partial^2 F_A(\Phi)/\partial\Phi^2(1-f_A^c)^3 \quad \text{at } T = T_c \text{ and } \Phi = f_A^c. \tag{19}$$

The full MCT predicts that there is one common component-independent λ for all chemical constituents of the system, a relationship well documented for binary systems, e.g., [26,27]. The exponents a, b, and γ follow from λ by

$$\lambda = \Gamma^2(1-a)/\Gamma(1-2a) = \Gamma^2(1+b)/\Gamma(1+2b), \tag{20}$$

$$\gamma = 1/2a + 1/2b \tag{21}$$

($0.5 \leqslant \lambda \leqslant 1$, $a < 0.395$, $0 \leqslant b \leqslant 1$). γ governs the temperature dependence of τ_α according to

$$\tau_\alpha \propto (T - T_c)^{-\gamma} \tag{22}$$

when approaching T_c from above. Moreover, the F_{12} model yields for the KWW exponent β the approximation [39,40]

$$\beta = \frac{\ln 2}{\ln(1-\lambda)}, \tag{23}$$

while, on the other hand, in the large-q limit the asymptotic result $\beta \to b$ is expected.

We here follow the basic lines of the MCT, but like in [10,11] we treat the memory kernel $F_A(t)$ as an unknown function, which can be calculated from the Laplace transforms of Eq. (11) and of $\Phi_A(t)$, once the latter is known, e.g., from MD simulations. (In the following the suffix A shall be skipped for brevity. The relations hold in all cases for one specific correlator and memory kernel, characterized by component index A and wave vector q.) Using the notation

$$\Phi_c(\omega) + i\Phi_s(\omega) = \lim_{\eta \to 0} L\{\Phi\}_{\eta - i\omega} \tag{24}$$

for the Laplace transform, one obtains

$$F(t) = (2/\pi)\int_0^\infty d\omega F_c(\omega)\cos(\omega t), \tag{25}$$

$$\omega F_c(\omega) = \frac{\omega\Phi_c(\omega)}{[1-\omega\Phi_s(\omega)]^2 + [\omega\Phi_c(\omega)]^2}. \tag{26}$$

Therefrom a function $F(\Phi)$ is constructed by relating to each $\Phi(t)$ the value $F(t)$, where $F(\Phi)$ is single valued if $\Phi(t)$ is monotonic in t. Our approach proceeds by introducing the g_m parameter [10,11,44], the maximum value of the function

$$G(\Phi) := F(\Phi)(\Phi^{-1} - 1), \tag{27}$$

$$g_m := \max\{G(\Phi) | 0 < t < \infty\}. \tag{28}$$

Below we use the notation Φ_m for the Φ value at which the maximum occurs, which means

$$\partial G(\Phi)/\partial\Phi = 0 \quad \text{at } \Phi = \Phi_m. \tag{29}$$

If $g_m < 1$, there is no arrested solution and the system is in the liquid state. $g_m \geqslant 1$ announces that the system can reach the arrested state. Therefore, g_m can be used as a measure of the extent to which the system has approached the arrested state. Following the treatment in [10,11], we shall use the temperature dependence of $g_m(T)$ as an indication of how the system approaches this state and as a means to estimate the critical temperature T_c.

As a particular test of our estimates of $F(\Phi)$ and the applicability of our approach, we shall compare $F(\Phi)$ with its Taylor expansion around Φ_m at temperature close to T_c:

$$f(\Phi) = F(\Phi_m) + F'(\Phi_m)(\Phi - \Phi_m) + 1/2F''(\Phi_m)(\Phi - \Phi_m)^2 + \cdots. \tag{30}$$

According to Eqs. (27) and (28), $F(\Phi_m)$ and $F'(\Phi_m)$ can be determined from knowledge of g_m and Φ_m:

$$F(\Phi_m) = g_m/(\Phi_m^{-1} - 1), \tag{31}$$

$$F'(\Phi_m) = g_m/(1-\Phi_m)^2. \tag{32}$$

$F''(\Phi_m)$ is determined by the exponent parameter λ, which means by the time evolution of the system, as visible, e.g., by the parameter γ. Comparison of $f(\Phi)$ with $F(\Phi)$, therefore, means a test whether, e.g., the temperature dependence of the system, Eq. (22), can be related to the estimated $F(\Phi)$.

III. SIMULATION RESULTS AND DISCUSSION

A. Enthalpy and specific heat

In this section, we report MD-simulated thermodynamic properties of $Cu_{60}Ti_{20}Zr_{20}$ alloy. Figure 2 demonstrates the enthalpy per atom as a function of temperature. Clearly, there is break in the slope of the enthalpy curve, which indicates the glass temperature T_g corresponding to the chosen cooling rate.

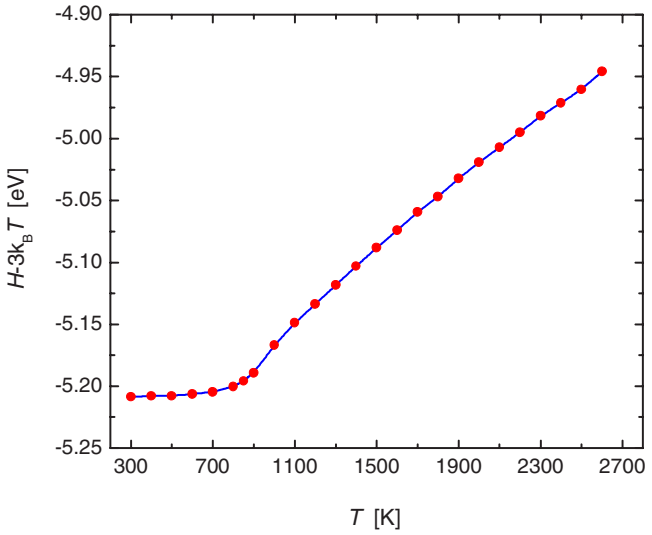

FIG. 2. (Color online) Reduced enthalpy of simulated amorphous $Cu_{60}Ti_{20}Zr_{20}$ versus temperature.

By differentiating the enthalpy H with respect to temperature, we obtain the specific heat at constant pressure, C_p, presented in Fig. 3. In the high-temperature range of 1200–1700 K, C_p increases slightly with decreasing temperature, which is the normal behavior of an equilibrium liquid [42]. In the range of 1000–1200 K, a sharp increase of the specific heat is seen. Such a sharp increase of the specific heat also is well settled by experiments [43]. Below 900 K, C_p decreases with reduction of temperature, which is taken as an indication that the system begins to fall out of equilibrium. Below 500 K, C_p changes almost linearly with temperature and tends to take on the classical Dulong-Petit value expected for harmonic solids ($C_p \approx 25$ J mol^{-1} K^{-1}). The simulation results indicate a glass transition regime between about 850 K and 600 K. Linear extrapolation of the low-temperature behavior and the decay between 800 K and 900 K yields an intersection at 753 K, which we interpret as the apparent glass transition temperature for the present cooling rate. This estimate is close to the experimental one, $T_g^{\text{expt}}=710$ K [5]. With respect to our necessarily large cooling rates, this agreement seems astonishing on the first glance. One has to realize, however, that we estimated T_g from the specific heat under cooling, while experimentally usually the curve under heating is analyzed. Due to hysteresis effects, T_g from cooling is expected at markedly lower temperatures than its estimate from heating, leaving sufficient space for cooling rate effects between our value and the experimental one.

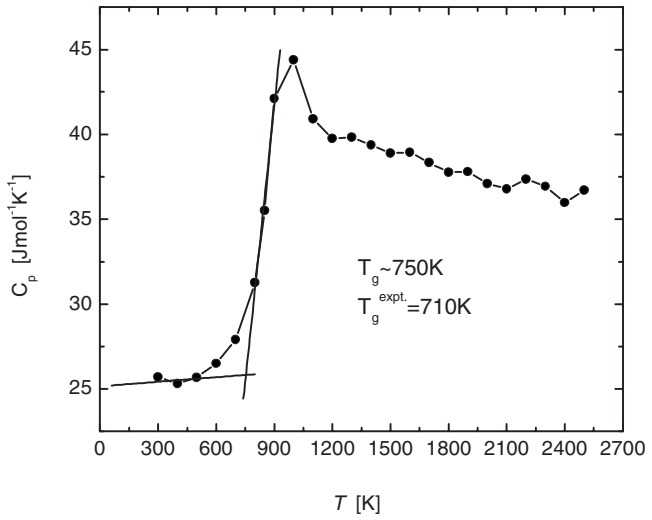

FIG. 3. Specific heat of simulated amorphous $Cu_{60}Ti_{20}Zr_{20}$ versus temperature.

B. Partial radial distribution function

By analyzing the radial distribution function, we obtained some information about the chemical short-range order in the $Cu_{60}Ti_{20}Zr_{20}$ melt. The calculated partial radial distribution functions (RDFs) $g_{ij}(r)$ at 300 K are shown in Figs. 4(a) and 4(b). There are some interesting features in the partial RDFs. First, there is a pronounced second peak in the Ti-Ti and Zr-Zr pairs, indicating that Ti-Ti and Zr-Zr have strong intermediate-range (IR) order. Compared to this, Cu-Cu seems to have weak or normal IR order. Second, Cu-Cu, Cu-Ti, and Cu-Zr pairs have a split in the second peak, which is not the case of Ti-Ti, Ti-Zr, and Zr-Zr pairs.

From integration of partial densities up to the first minimum in the radial distribution function, we obtain the coordination numbers Z_{ij} listed in Table III. According to the data of Table III, Cu has a total of 11.2 neighboring atoms. (Note that $x_i Z_{ij}=x_j Z_{ji}$, with x_i and x_j the fractions of i and j particles in the system.) In a random system, one would expect Cu to have 60% Cu neighbors, which means 6.7, while the simulations give 4.77. This means that Cu has an increased affinity to Ti and Zr atoms. This tendency can be easily seen from the projection of a configuration at 300 K shown in Fig. 5. There it looks as if one- and two-dimensional arrangements of Zr and Ti atoms are wrapped by shells of Cu atoms, which provide the interaction between the different Zr-Ti groups.

Like the recently analyzed simulation data for the ternary bulk glass-forming $Al_{15}Ni_{25}Zr_{60}$ [7], the present results for $Cu_{60}Ti_{20}Zr_{20}$ indicate a rather complex structure with significant intermediate-range order. There is, however, a marked difference between the present findings and the previous ones, which obviously reflects differences in the interatomic couplings of the two systems. The present system is characterized by the fact that among the atoms of the majority component Cu, there is only a negligibly weak attractive pair interaction with the main part of cohesion coming from the indirect electron gas pressure. In the former $Al_{15}Ni_{25}Zr_{60}$ system, Zr atoms form the majority component which thus is characterized by strongly attractive covalent pair interactions. According to that, in the Zr-dominated structure the minority Al and Ni atoms reside in suitable polyhedral cages within a rigid Zr matrix. Al is found in icosahedral holes, Ni mainly in trigonal-prismatic environments. An additional IR order arises in the structure as Al atoms prefer to form short stringlike structures with Al-Al neighbors while the Ni atoms with their trigonal-prismatic cages form strings that avoid direct Ni-Ni contacts. The global IR of amorphous

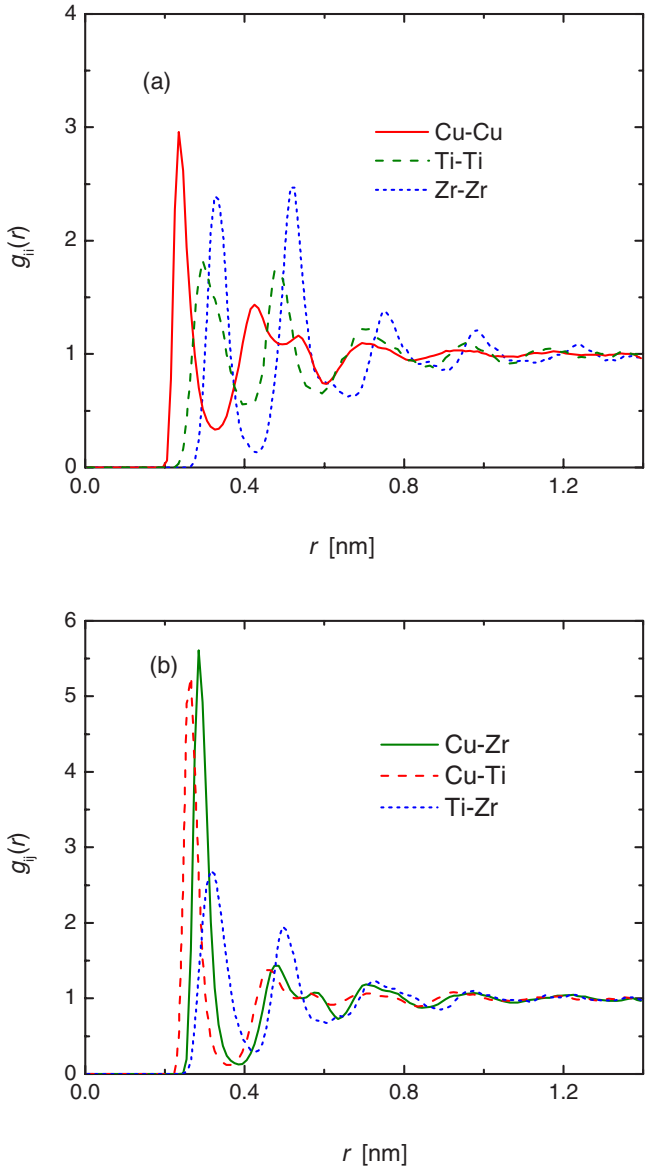

FIG. 4. (Color online) Partial radial distribution function of simulated $Cu_{60}Ti_{20}Zr_{20}$ in the glassy state at 300 K.

$Al_{15}Ni_{25}Zr_{60}$ then follows from combining these structural elements in a space-filling way. In the present case, for the $Cu_{60}Ti_{20}Zr_{20}$ system, the IR structure seems much more flexible than in the Zr-dominating melt, probably due to the flexibility in the Cu subsystem, which acts like glue with strong adhesion to the Ti and Zr atoms but minor rigidity within the Cu sheets.

TABLE III. Nearest-neighbor distances d_{ij} and mean coordination numbers Z_{ij} of atoms type j around atoms of type i in amorphous $Cu_{60}Ti_{20}Zr_{20}$ at 300 K.

	d_{ij} (Å)	Z_{ij}
Cu-Cu	2.35	4.77
Ti-Cu	2.65	8.53
Zr-Cu	2.85	10.76
Ti-Ti	2.95	3.0
Ti-Zr	3.15	3.92
Zr-Zr	3.25	2.96

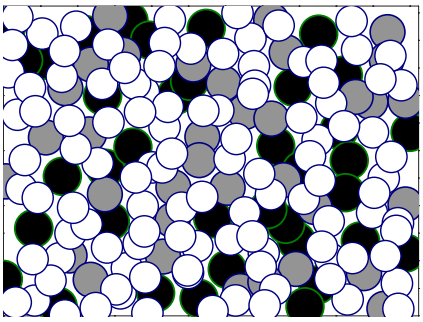

FIG. 5. (Color online) Projection of the configuration at 300 K. The thickness of the projected slice is 5 Å. The dark, gray, and white balls represent Zr, Ti, and Cu atoms, respectively. The vertical box length is 2.756 nm.

The evolution of structure is analyzed by investigating the temperature dependence of six partial RDFs shown in Fig. 6. There we observe a split of the second peak in the Cu-Cu, Cu-Ti, and Cu-Zr RDFs at a temperature around 1000–1100 K and below, which means an increased short-range order compared to higher T. Interestingly, the sharp increase of specific heat also occurs in this temperature range. There may be some relationship between the pronounced short-range order and the sharp increase of the specific heat. In fact, the liquid with pronounced short-range order has lower energy than the normal one, which leads to a larger temperature dependence of the enthalpy. This argument gives a way to understand why the specific heat undergoes a sharp increase with decreasing temperature, which just begins when the splitting of the second peak starts.

C. Mean-squared displacements and self-diffusion coefficient of $Cu_{60}Ti_{20}Zr_{20}$ alloy

MSDs were investigated for the three species Cu, Ti, and Zr at different temperatures. Since the MSD for the different species shows similar features, we display for illustration only the MSD of Cu atoms in Fig. 7. At higher temperatures, the MSD can be divided into two regimes, the ballistic regime and the diffusive. At lower temperatures, approaching T_g, there appears a plateau at intermediate times, which becomes larger with decreasing temperature and extends over several decades in time at the lowest temperature. The plateau reflects the fact that the moving particle is temporarily arrested in a cage formed by the neighboring atoms. With the decrease of temperature, this cage becomes more rigid and can be broken up only after increasingly long-time periods.

From the first derivative of the MSD in the diffusive regime, the self-diffusion coefficients for the three species were evaluated. The results are shown in Fig. 8. In the liquid phase the coefficients decay with decreasing temperature in a super-Arrhenius manner, in agreement with experiments [44] and simulations for structural glass-forming models like $Ni_{50}Zr_{50}$ [44,45], $Ni_{20}Zr_{80}$ [11], $Cu_{50}Zr_{50}$ [44], or the Lennard-Jones system [23]. In order to test the predictions of

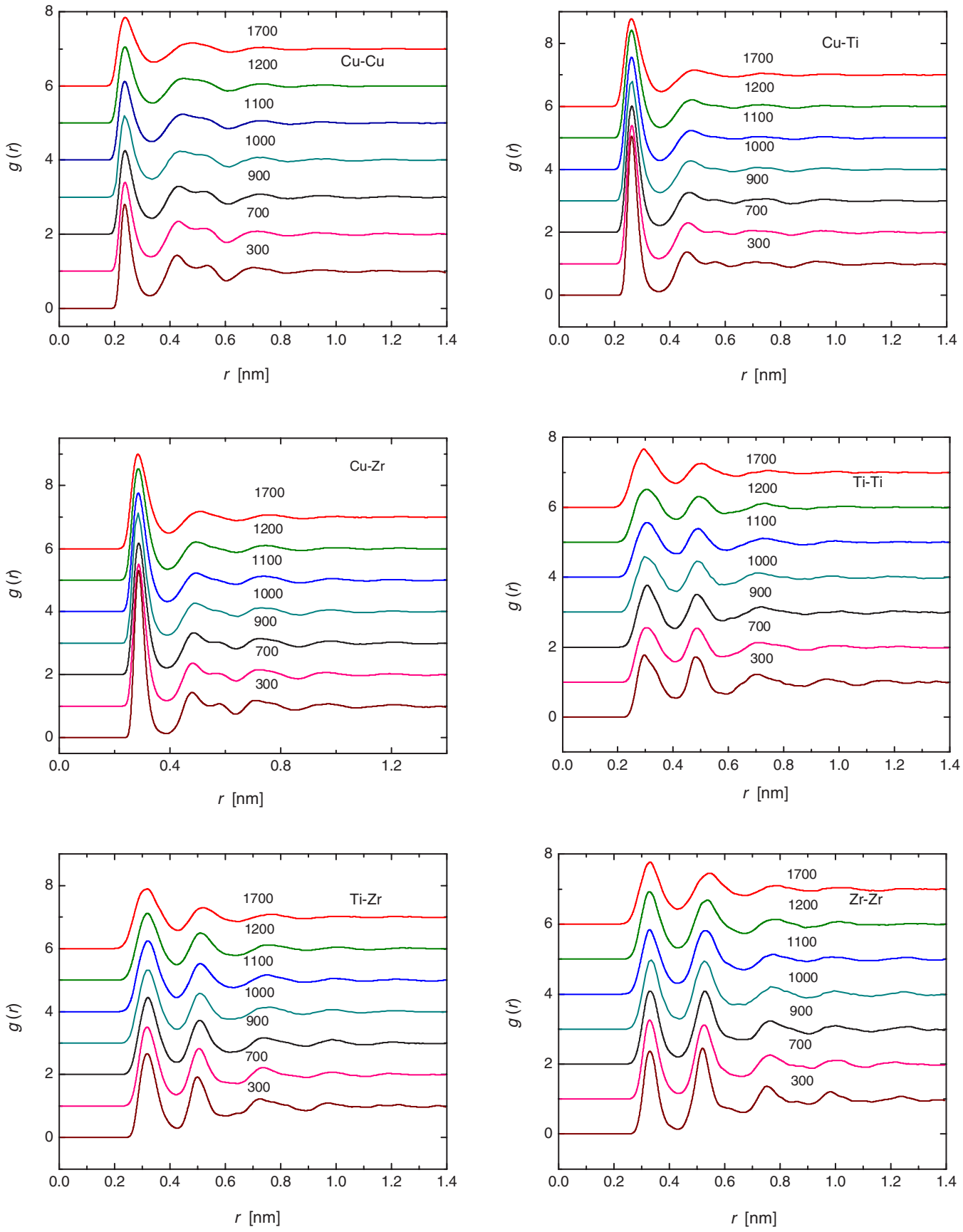

FIG. 6. (Color online) Partial radial distribution functions of the six pairs in simulated $Cu_{60}Ti_{20}Zr_{20}$ alloy at different temperatures.

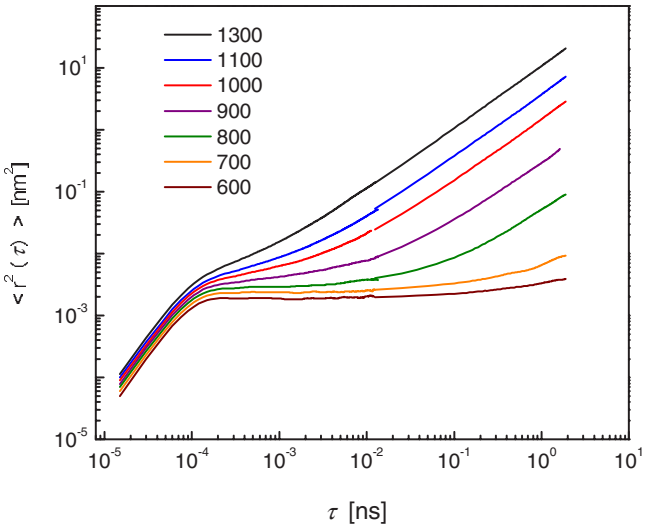

FIG. 7. (Color online) MSD of Cu atoms at different temperatures in simulated $Cu_{60}Ti_{20}Zr_{20}$.

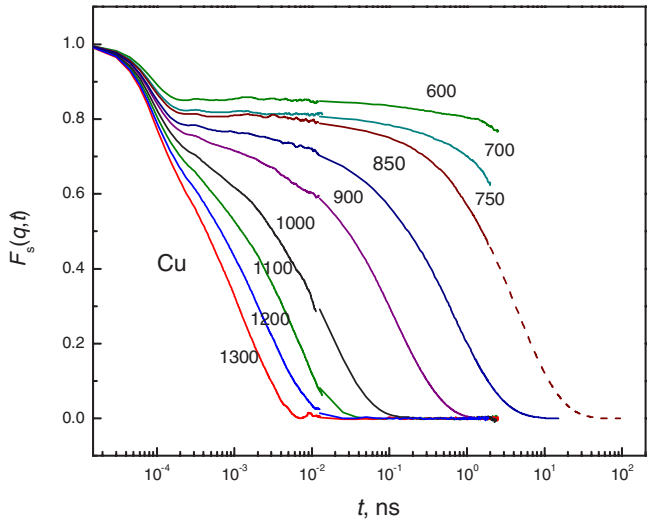

FIG. 9. (Color online) Intermediate scattering function $\Phi(q,t)$ of Cu in simulated $Cu_{60}Ti_{20}Zr_{20}$ at different temperatures.

the MCT [34] for the self-diffusion coefficient, we approximated their temperature dependence by the MCT power law, Eq. (8). Figure 8 demonstrates that Eq. (8) can describe the self-diffusion coefficient of the three species quite well in the temperature range down to 950 K. Data analysis gives a T_c value of 870 K for three species and γ values of 1.66, 1.69, and 1.62 for Cu, Ti, and Zr, respectively. However, the exponents γ are clearly below the lower limit $\gamma_c \approx 1.765$ set by MCT through Eq. (21). The deviation from the MCT prediction found here has its counterpart in earlier simulations, like for the Lennard-Jones model [23] or the $Ni_{50}Zr_{50}$ [45]. The γ values found there are above γ_c, but they deviate from the prediction of Eq. (21), which fixes γ when knowing one of the parameters a or b from an independent "measurement."

The self-diffusion coefficients are also fitted using the empirical VFT law [35–37]. The results are included in Fig. 8 by dashed lines. Figure 8 demonstrates that the VFT law

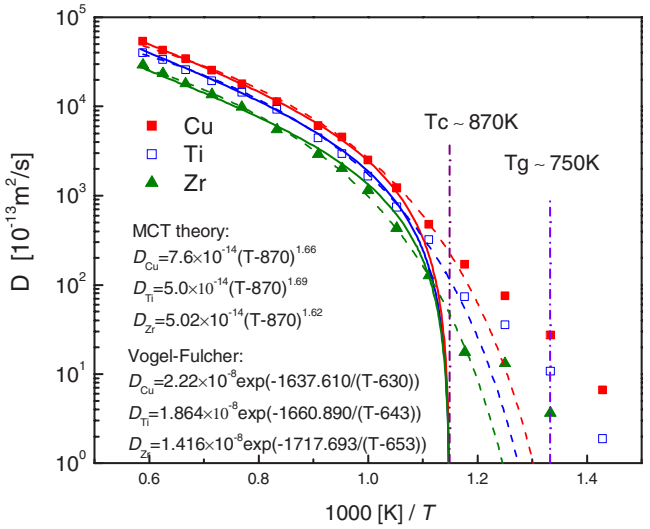

FIG. 8. (Color online) Self-diffusion coefficients of three constituents in simulated $Cu_{60}Ti_{20}Zr_{20}$ alloy at different temperatures, including MCT and VFT fit curves.

represents the self-diffusion coefficients well above 850 K. Data regression gives a T_0 value of 630, 643, and 653 K for Cu, Ti, and Zr, respectively. The corresponding B values are 1637.610, 1660.890, and 1717.693, respectively. The limiting temperature of 850 K is close to the MCT T_c, but as already mentioned, this temperature marks for our system also the onset of its falling out of equilibrium under the applied cooling rate. Regarding this, the coincidence with T_c might be an accidental one, reflecting the fact that our T_g is rather close to T_c. The present finding has to be seen in context with the results by Kob and Andersen [23] for the Lennard-Jones system, where the MCT formula turned out superior to the VFT relationship when restricting to temperatures $T \geqslant 1.07T_c$. Our analysis shows that the VFT law gives a fair representation of the D_A down to T_c.

D. Incoherent intermediate scattering function $\Phi(q,t)$

In order to characterize the time evolution of the ternary system in more detail, we have analyzed the intermediate scattering function $\Phi(q,t)$ for the three components Cu, Ti, and Zr. Since they exhibit similar characteristics, we present in Fig. 9 the ISF only for Cu at different temperatures for a wave vector of $q_{10}=22.4$ nm^{-1}, which corresponds to the first peak of the total radial distribution function $r \approx 2.8$ Å in r space.

The behavior of the ISF is the one well known from experiments [46] and simulation [9,15,24,41]: For short times, $\Phi(q,t)$ shows a Gaussian-type dependence on time, which is consistent with the ballistic motion of the particles. At high temperatures a further decay takes place, which is close to an exponential decay, as can be inferred from the fact that for high T the non-Gaussian parameter in general is small and the MSD approaches diffusive behavior.

As temperature decreases, there appears a small shoulder in the intermediate-time range, indicating the beginning formation of the β regime. When the temperature decreases to about 850 K, this shoulder develops into a plateau, which

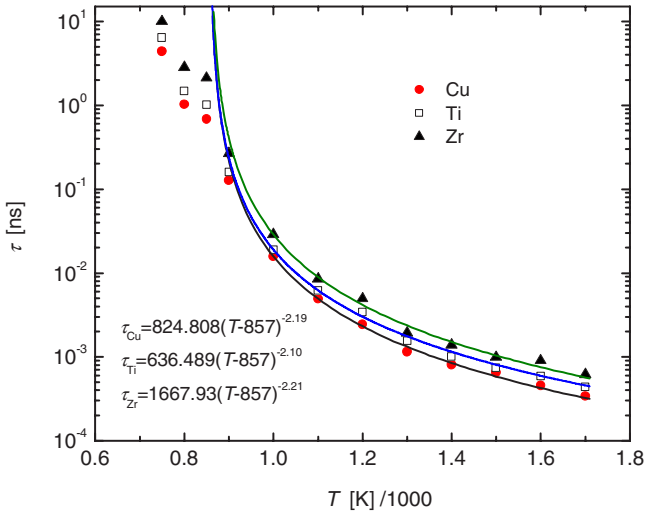

FIG. 10. (Color online) α-relaxation time for the three components in simulated $Cu_{60}Ti_{20}Zr_{20}$ at different temperatures.

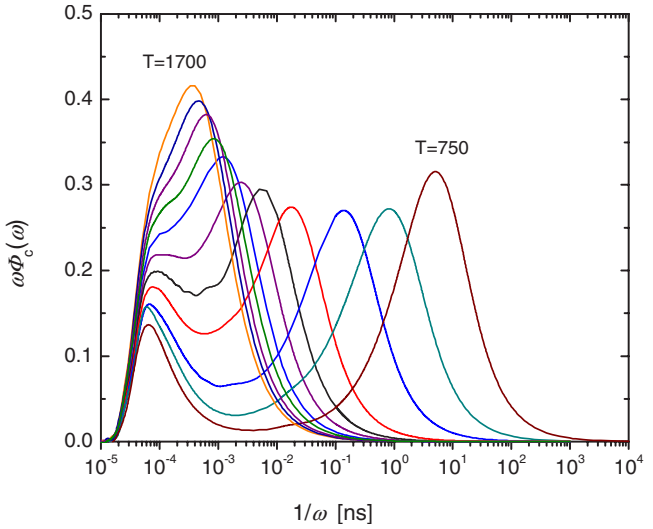

FIG. 11. (Color online) Dynamical susceptibility of Cu at different temperatures in simulated $Cu_{60}Ti_{20}Zr_{20}$. Curves from left to right correspond to temperatures of 1700, 1600, 1500, 1400, 1300, 1200, 1100, 1000, 900, 850, and 750 K.

extends further with further decrease of temperature. For this late β relaxation regime, MCT yields that the ISF can be described by the von Schweidler law, Eq. (14), which turns into the final α decay, for which MCT gives the KWW relationship, Eq. (18), as a useful approximation.

Figure 10 presents the temperature dependence of τ_α, where τ_α is obtained by fitting the KWW law to the MD data of the ISF. MCT predicts for the temperature dependence of τ_α a critical behavior with exponent $-\gamma$ as given by Eq. (22). In Fig. 10, the lines present curves of the form of Eq. (22) fitted to the τ_α values. Clearly, expression (23) can describe very well the temperature dependence of τ_α above T_c, with $T_c=857$ K for three species and γ values 2.19, 2.10, and 2.21 for Cu, Ti, and Zr, respectively. These γ values are larger than the values derived from the self-diffusion coefficient and are clearly above the critical value γ_c of MCT.

E. Dynamical susceptibility

The dynamical susceptibility $\chi''(\omega)=\omega\varphi_c(\omega)$ of the $Cu_{60}Ti_{20}Zr_{20}$ ternary alloy was computed from the cosine-Fourier transformation of the ISF. For demonstration, the dynamical susceptibility of the Cu atoms at different temperatures is presented in Fig. 11. The figure shows that at high temperatures (curves to the left) there is only one peak and it is located at microscopic frequencies. As the temperature decreases, this peak splits gradually into two. One stays at the microscopic frequencies; the other, the α-relaxation peak, moves towards low frequencies with the decrease of temperature.

MCT predicts that the position of α-relaxation peak, ω_{max}, follows a power law of temperature:

$$\omega_{max} \propto (T-T_c)^\gamma, \tag{33}$$

with γ according to Eq. (21). As illustrated in Fig. 12, this prediction holds quite well in our case. Data fitting results in $T_c=855$ K for the three species and the γ values are 2.225, 2.156, and 2.145 for Cu, Ti, and Zr, respectively. These γ values are quite close to those derived from τ_α.

The β relaxation takes place in the frequency range between high-frequency microscopic dynamics and low-frequency α decay. In this range, there is a minimum in χ'', whose position and value we denote by ω_{min} and χ''_{min}, respectively. MCT predicts the relationship [20]

$$\chi''_{min} \propto (T-T_c)^{1/2}. \tag{34}$$

In Fig. 13, we present χ''_{min} versus $T-T_c$ in a double-logarithmic plot. Linear regression gives a critical temperature of 865 K and exponents 0.52443, 0.52637, and 0.57374 for Cu, Ti, and Zr, demonstrating that the prediction of MCT, Eq. (34), holds well in the bulk-glass-forming ternary $Cu_{60}Ti_{20}Zr_{20}$ melt.

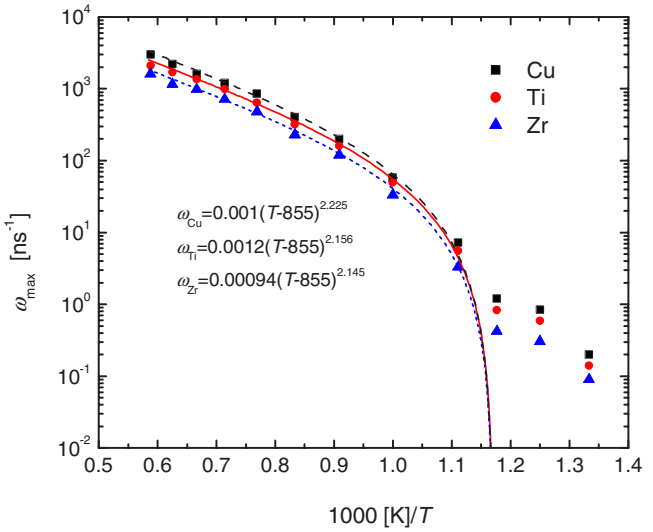

FIG. 12. (Color online) Position of the α-relaxation frequency peak versus temperature in simulated $Cu_{60}Ti_{20}Zr_{20}$.

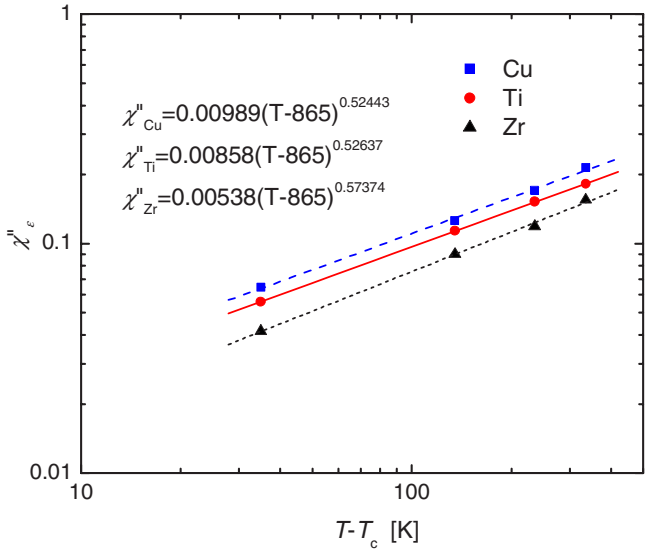

FIG. 13. (Color online) Value of the minimum in the β-relaxation regime versus $T-T_c$ in simulated $Cu_{60}Ti_{20}Zr_{20}$.

F. Memory kernel $F_A(\Phi)$

According to Sec. II, the frequency-dependent memory kernel $F_A(\omega)$ can be evaluated from Laplace transformation of the evolution equation (11) and of $\Phi_A(t)$. As to be expected from the mentioned similarity of the ISFs for Cu, Ti, and Zr, the $F_A(\omega)$ turned out to be rather similar. For demonstration, we display in Fig. 14 the results for Cu at various temperatures (wave vector $q=22.4$ nm^{-1}) obtained from the ISF of Fig. 9. In agreement with the observation for $Ni_{50}Zr_{50}$ [10], the figure shows marked contributions to $\omega F_c(\omega)$ in those frequency ranges where the susceptibility $\chi''(\omega)$ has large amplitudes.

Fourier transformation of $F_c(\omega)$ allows one to determine $F(t)$. Therefrom we have constructed the function $F(\Phi)$ for Cu, Ti, and Zr, Fig. 15, by plotting $F(t)$ vs $\Phi(t)$. At low values of Φ (below about 0.5) $F(\Phi)$ is only weakly temperature dependent and shows a monotonic increase. From Fig. 15 it is obvious that for Φ values below the limit of about 0.5 the function $F(\Phi)$ may be well approximated by a polynomial $P(\Phi)$ as assumed by MCT. On the other hand, for Φ values around and above 0.8, there are marked deviations from the low-Φ behavior, where the onset of the deviation shifts to lower Φ the higher the temperature is. The Φ range of deviation from low-Φ behavior agrees with the regime of the initial decay of the ISF due to the atomic vibrations. This can be seen by comparing the plot of the ISF $\Phi_{Cu}(t)$, Fig. 9, and the $F_{Cu}(\Phi)$ dependence, Fig. 15. Our observation thus reconfirms the earlier finding for $Ni_{50}Zr_{50}$ [10], that the polynomial approach for $F(\Phi)$, proposed and analyzed in the schematic MCT, is not applicable in the range of the structural decay by atomic vibration. In particular, the present approach predicts at low temperatures a rather sharp boundary $\Phi_b(T)$ above which the MCT predictions will not be valid. While the sharp boundary $\Phi_b(T)$ at lower temperatures is given from the abrupt break in the slope of $F_{Cu}(\Phi)$, it turns into a smooth deviation from the MCT results at higher temperatures—e.g., 1100–1300 K in Fig. 15.

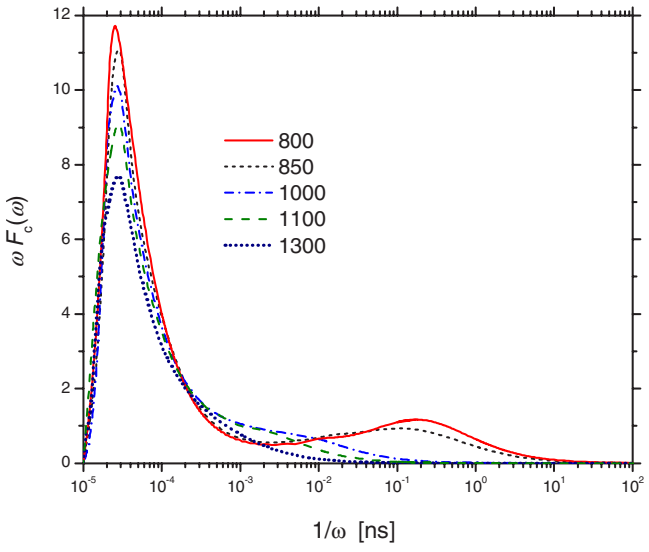

FIG. 14. (Color online) Spectral distribution $\omega F_c(\omega)$ for the memory kernel of Cu in simulated $Cu_{60}Ti_{20}Zr_{20}$.

G. Estimate of T_c from $g_m(T)$ and test of the present approach

Following the method of [10,11,41], we estimate here the critical temperature T_c from analyzing the properties of $G(\Phi)$, Eq. (27), as described in Sec. II. In Fig. 16, we present the temperature dependence of $g_m(T)$, the maximum of $G(\Phi)$, for the three components of our ternary $Cu_{60}Ti_{20}Zr_{20}$ alloy. There are two distinct linear temperature ranges visible in Fig. 16. As temperature decreases at temperatures higher than 850 K, g_m increases linearly towards the value of 1 with a large slope. Below 850 K, g_m remains close below the limiting value of 1 and increases slightly and linearly with decrease of temperature.

This behavior is similar to that observed in simulations for $Ni_{50}Zr_{50}$ [10] and $Ni_{20}Zr_{80}$ [11]. It indicates that all systems analyzed avoid a sharp crossover and the entrance into the arrested state by remaining below the $g_m=1$ borderline. This is taken as an indication of more complex correlated dynamical many-body processes, such as transversal currents or collective thermal excitations, not fully taken into account in the approximate memory kernel of MCT (compare [26,27]) or the temperature dependence of the λ_1 and λ_2 parameters in the schematic MCT.

We here use an extrapolation of the $g_m(T)$ values above 850 K to estimate an apparent T_c value for the simulated melt and to map its properties above this value to the predictions of the schematic MCT. Linear fit of g_m values for Cu, Ti, and Zr atoms above 850 K predicates a crossover temperature T_c^* from liquid ($g_m<1$) to quasiarrested ($g_m\rightarrow 1$) behavior around 851 K for Cu, 856 K for Ti, and 858 K for Zr. We estimate T_c as 855 K from the mean value of these three T_c^*. As demonstrated by Table IV, this value agrees with the ones estimated from the position of α-relaxation peak (Fig. 12) and from $\omega_{max}(T)$, giving additional substantiation to the assumption of Ref. [11] that all these methods can be used equally well to estimate T_c.

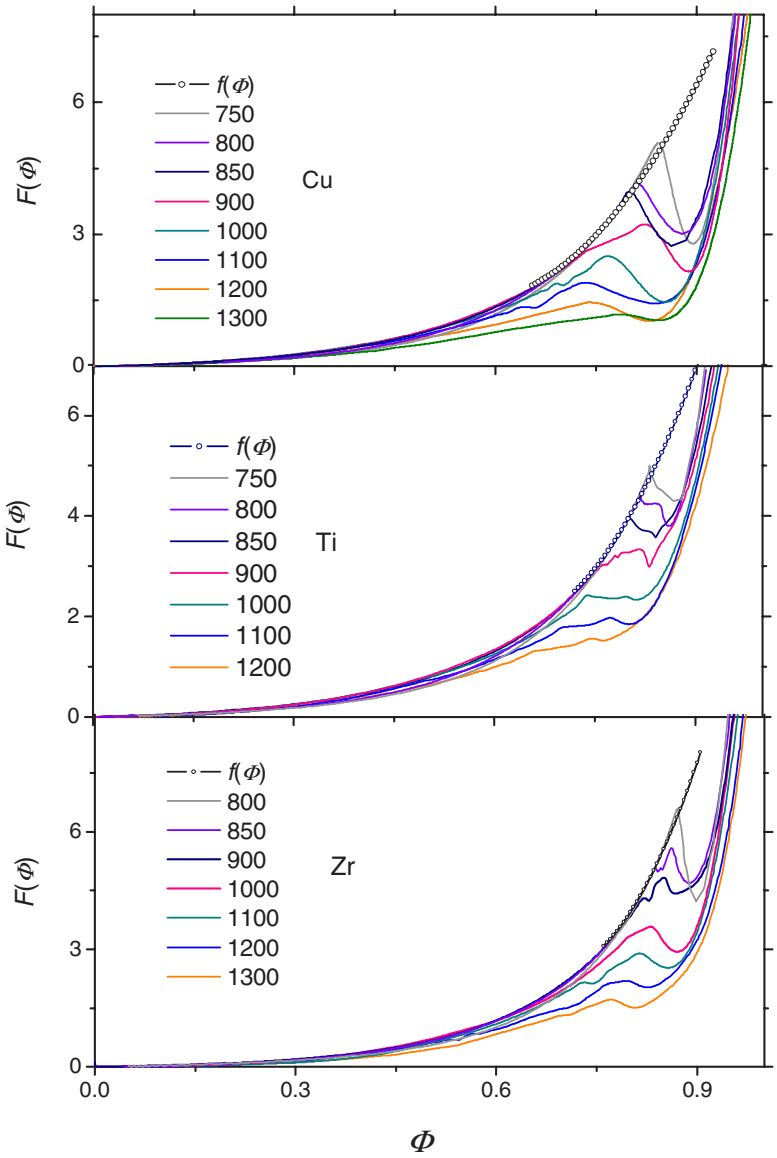

FIG. 15. (Color online) $F(\Phi)$ at various temperatures and its Taylor expansion $f(\Phi)$ at 850 K for Cu, Ti, and Zr in simulated $Cu_{60}Ti_{20}Zr_{20}$. [With increasing temperature the kink or intermediate maximum in the $F(\Phi)$ curves shifts to lower F values.]

As indicated in Sec. II, by comparing $F(\Phi)$ with its Taylor expansion $f(\Phi)$ around Φ_m, Eq. (30), we can test the consistency between our calculated $F(\Phi)$ and the prediction of the schematic MCT for the time evolution of the correlator $\Phi(t)$. According to Eqs. (31) and (32), $F(\Phi_m)$ and $F'(\Phi_m)$ are fully determined by g_m and Φ_m. The MCT predicts that $F''(f^c)$ can be estimated from the exponent parameter λ and the critical correlator f^c, Eq. (19). Consistency between our approach and MCT implies in particular $\Phi_m(T_c)=f^c$, which means we may deduce $F''(\Phi_m)$ from λ by identifying f^c with $\Phi^m(T_c)$ in Eq. (19).

The value of λ is estimated from the exponents γ by means of Eqs. (21) and (22). For evaluating λ we take into account the γ exponents from the temperature dependence of τ_α and $\omega_{\max}$, compiled in Table V, leaving aside the data from the diffusion coefficients. Regarding the scattering of the two values for each species and the rather close agreement between the man values for the three components, it seems natural to deduce from the γ values a component-independent mean $\langle\gamma\rangle==2.17$, yielding $\lambda=0.661$ and $a=0.342$, $b=0.705$. The assumption of a component-independent λ is in agreement with the results of the full MCT. As presented in a number of studies for binary systems [24,39,40] MCT predicts the existence of one and the same λ for the different species. There are no serious doubts that the arguments providing the component-independent λ in the binary case will not hold for the ternary system, too. Table V also compiles the further data needed for constructing the Taylor expansion $f(\Phi)$.

The resulting second-order expansions $f(\Phi)$ around Φ_m(850 K) are included in Fig. 15. For all three species, the plot demonstrates good agreement between $F(\Phi)$ and $f(\Phi)$ for Φ close to Φ_m. The deviations between the functions $F(\Phi)$ and the series expansions $f(\Phi)$ at lower Φ are due to our being limited to a second-order approach. The deviation at values well above Φ_m may be due to uncertainties in the evaluation of $F(\Phi)$ at 800 K and 750 K. Evaluation of $F''(\Phi_m)$ from $\langle\gamma\rangle$ and λ, respectively, depends significantly on a proper estimate of f_c. Regarding this sensitive dependence, the agreement between $F(\Phi)$ and $f(\Phi)$ must be taken

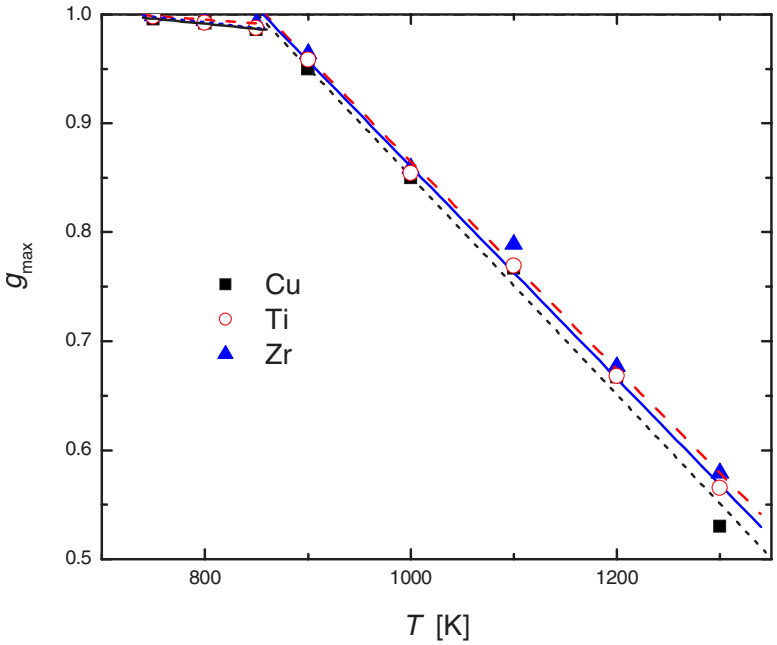

FIG. 16. (Color online) g_{max} for the three constituents in simulated $Cu_{60}Ti_{20}Zr_{20}$ as a function of temperature.

as a great demonstration of the consistency between the approaches used.

In the α-decay regime, $\Phi(t)$ can be well represented by the KWW law, Eq. (18), with suitably chosen amplitude A_0, relaxation time τ_α, and exponent β. Around T_c, the amplitude A_0 should be close to f_c. Applicability of the KWW law with this amplitude is demonstrated by Fig. 17 for Cu, Ti, and Zr, where the simulation data are shown for $T=850$ K and, by dashed line, the KWW approximation. In Fig. 17, the straight lines in the α-decay regime describe for each component the tangent to the KWW law vs $\ln(t)$ at τ_α with slope $-\beta f_c e^{-1}$. The corresponding β values are included in Table V. The values are rather close to each other, ranging from 0.678 for Cu to 0.650 for Ti. They are not too far away from the asymptotic MCT result in the large-q limit, $\beta \to b=0.705$, and they are close to the value $\beta=0.64$ following from the approximation, Eq. (23), when using for λ the mean value deduced above.

IV. SUMMARY AND CONCLUDING REMARKS

The present contribution reports results from MD modeling of the ternary, bulk metallic glass-forming $Cu_{60}Ti_{20}Zr_{20}$ system. As mentioned in the Introduction, the system was chosen as an example of a BMG-forming melt with rather promising technological features [5]. The present research was aimed at getting information on the microscopic properties of $Cu_{60}Ti_{20}Zr_{20}$ and at promoting our knowledge of glass-forming melts at all. Accordingly, we here provided results concerning basic properties of the $Cu_{60}Ti_{20}Zr_{20}$ undercooled melt, such as the partial radial distribution functions and nearest-neighbor numbers, specific heat, simulated glass temperature, or the diffusion coefficients. A second group of results is related to the fluctuation dynamics in time, visible, for example, in the intermediate scattering function, and the analysis of this function within the mode coupling theory. Here we considered the critical temperature T_c of MCT, tests of the MCT predictions concerning the time and temperature dependence of various quantities, and the evaluation of the apparent memory kernel that provides the damping of the dynamics in the complex, highly viscous structure.

First we will emphasize once again that our model reproduces well the experimentally determined total radial distribution of $Cu_{60}Ti_{20}Zr_{20}$ [33], which is a clear indication that the model meets well the steric conditions of the system. Regarding further details of the structure, our investigation shows that the present system differs significantly from that of the previously analyzed ternary $Al_{15}Ni_{25}Zr_{60}$ alloy [7], which is also an interesting BMG-forming system. The dif-

TABLE IV. Estimated values of T_c for simulated $Cu_{60}Ti_{20}Zr_{20}$ from different methods.

Estimating methods	T_c (K)
Self-diffusion coefficient	870
α-relaxation time	850
Position of α-relaxation peak	855
Minimum of β regime	865
Memory kernel	855

TABLE V. Data for constructing the Taylor expansion $f(\Phi)$ for Cu, Ti, and Zr from simulation of $Cu_{60}Ti_{20}Zr_{20}$ at 850 K and estimated γ values. β from the KWW law.

	Cu	Ti	Zr
g_m	0.987	0.989	0.992
Φ_m	0.75634	0.7815	0.8238
$\gamma(\omega_{max})$	2.225	2.156	2.145
$\gamma(\tau_\alpha)$	2.19	2.10	2.21
β	0.6782	0.650	0.663

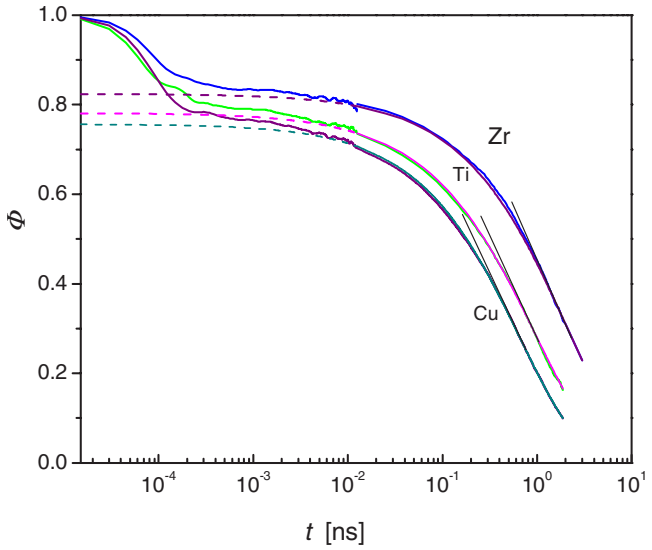

FIG. 17. (Color online) ISF for Cu, Ti, and Zr at 850 K in simulated $Cu_{60}Ti_{20}Zr_{20}$ and the KWW law, Eq. (18), for each component with β and $A_0=\Phi_m$ from Table V. The straight lines in the α regime are the tangents to the KWW law vs $\ln(t)$ at τ_α.

ference in structure seems due to the fact that in the present material the Cu atoms form the majority component, which have only weak couplings among each other but strong covalent bonding to the minority components Ti and Zr. Accordingly, the majority atoms act like flexible glue that holds tightly together groups of strongly bound Ti and Zr atoms. The overall structure seems to be built by groups of Ti and Zr atoms wrapped by sheets of Cu atoms, which provide the coupling between the Ti-Zr groups. In contrast to this, in the Zr-based $Al_{15}Ni_{25}Zr_{60}$ structure, the majority component of Zr atoms forms a rigid matrix, within which the Al and Ni atoms are immersed in well-defined polyhedral cages. The intermediate-range structure in this material is determined by the relative arrangement of these cages.

Despite the significant differences in details of the structure, the present ternary $Cu_{60}Ti_{20}Zr_{20}$ and the earlier $Al_{15}Ni_{25}Zr_{60}$ systems have in common that they display a complex intermediate-range structure, which reflects a complicated interplay between the short-ranged chemical bonding between the three components, steric conditions enforced by the size of the components, and optimization of the chemical potential when forming the space filling structure.

The analysis of the intermediate scattering function in terms of MCT and its modification [10,11] shows that the present ternary $Cu_{60}Ti_{20}Zr_{20}$ behaves in this respect like the common binary glass-forming melts—e.g., the NiZr alloys [10,11] or the Lennard-Jones model [24]. We have in particular deduced that the present system fulfills well the predictions of MCT concerning the existence of a common exponent parameter λ for the different chemical components and the interrelationship between the λ parameter and the critical exponent γ that governs the temperature dependence of the α-relaxation time τ_α or the shift of the α-relaxation frequency peak ω_α above T_c.

In contrast to this agreement with the results of MCT, the algebraic t^{-a} decay predicted by MCT for the early β regime was not found for the present system, as it was not found in former MD studies of structural glasses and related systems [10,11,14,24]. Already in the early MD simulation by Lewis and Wahnström [15], the absence of this decay was attributed to masking effects by single-particle vibrations, not taken into account in MCT.

The present analysis provides direct confirmation of this argument from transforming the time dependence of the memory kernel $F(t)$ by use of $\Phi(t)$ into an $F(\Phi)$ relationship. For T around T_c, we find that only for Φ values below a critical Φ_b does the kernel $F(\Phi)$ have the smooth, polynomial-like Φ dependence assumed by the schematic MCT. Above that value, $F(\Phi)$ exhibits a rather different behavior. From comparison with $\Phi(t)$ it is obvious that the Φ range above Φ_b is just the range where the decay of the correlator $\Phi(t)$ with time is governed by the atomic vibrations. Since Φ_b is only slightly above the plateau value of the correlator, there is nearly no Φ range left for developing the t^{-a} decay. The existence of the boundary Φ_b and its meaning for the memory kernel are known already for Zr-rich NiZr systems [10,11], which are dominated by marked covalent bonding in the majority component of Zr atoms. The present study demonstrates that the same mechanism acts also in a metallic melt with simple-metal-like interactions among the majority atoms.

As an important by-product, our analysis predicts that the memory kernel $F(\Phi)$ for the correlator Φ can be constructed for T near T_c and Φ around the asymptotic nonergodicity parameter value f^c of the schematic MCT, when knowing the exponent parameter λ (e.g., from the γ exponents), the value of f^c, and the value of the g_m parameter at the apparent T_c. Within the assumptions of the schematic MCT, g_m takes on the borderline value 1 at T_c, while our analysis yields g_m values deviating from this borderline by the order of 10^{-2} at the effective T_c. With regard to that, a rough picture of $F(\Phi)$ around $\Phi=f^c$ can be gained already from knowing λ and the plateau value f^c, approximating, in Eq. (31), $g_m \approx 1$.

There is a further point to address. In our approach, we use g_m as the fundamental quantity to visualize how the melt approaches the arrested state. In accordance with the treatments for the binary NiZr melts [10,11,41], the present analysis shows a linear increase of g_m with decreasing temperature in a broad temperature range. This implies that the approach of the system towards the arrested state, indeed, is linear in the control parameter $\varepsilon=(T/T_c-1)$, up to a narrow regime close to T_c. For all systems analyzed by our method so far, the linear $(T-T_c)$ dependence extends over more than 500 K, where an upper limit has not yet been observed. This large region of proportionality explains why the predictions of MCT concerning the critical temperature dependences of the systems are applicable for a rather large range of the control parameter ε, up to values of ε around 0.5 and above.

In conclusion, our analysis has contributed information about the microscopic properties of the ternary BMG-forming $Cu_{60}Ti_{20}Zr_{20}$ melt, and it may help to promote our knowledge about the characteristic phenomena governing the physics in the range of the glass transition, especially around the critical temperature T_c of the MCT. We have shown that

TABLE VI. Comparison of calculated and experimental data for crystalline Zr, Ti, and Cu.

		Simulation	Experiment
Zr	a (nm)	0.324	0.323
	c/a	1.634	1.591
	E_{coh} (eV/atom)	5.79	6.25
	T_m (K)	2280	2125
Ti	a (nm)	0.299	0.295
	c/a	1.632	1.586
	E_{coh} (eV/atom)	5.46	4.85
Cu	a (nm)	0.369	0.361
	E_{coh} (eV/atom)	4.18	3.49

$Cu_{60}Ti_{20}Zr_{20}$, like the earlier investigated $Al_{15}Ni_{25}Zr_{60}$ [7], is characterized by a microscopic structure with marked intermediate-range order and that its dynamics fulfills in most respects the predictions of MCT [18–22], up to an absence of the algebraic t^{-a} decay in the early β regime. From evaluating the effective memory kernel $F(\Phi)$ of the system, this absence is traced back to deviations of $F(\Phi)$ from the approximate form analyzed in MCT, where a method to reconstruct around T_c major parts of $F(\Phi)$ from λ and the plateau value f^c turned out as a by-product of our investigation.

TABLE VII. Lattice constants a and c for crystalline $CuTi_2$, CuTi, $CuZr_2$, and CuZr from simulation and experiments.

	a (nm)		c (nm)	
	Simulation	Experiment	Simulation	Experiment
$CuTi_2$	0.281	0.294	1.0923	1.0786
CuTi	0.311	0.328	0.592	0.558
$CuZr_2$	0.332	0.322	1.0232	1.1183
CuZr	0.326	0.332		

ACKNOWLEDGMENTS

This work is financially supported by the Alexander von Humboldt Foundation. X.H. is grateful to M. Guerdane, I. Ladadwa, K. Brinkmann, and D. Marcano for beneficial discussions.

APPENDIX

Here we present some tests of the interaction potentials for the $Cu_{60}Ti_{20}Zr_{20}$ alloy. Table VI presents results for the monatomic crystalline Zr, Ti, and Cu systems, which test the Zr-Zr, Ti-Ti, and Cu-Cu interactions used here. Table VII presents results for crystalline $CuTi_2$, CuTi, $CuZr_2$, and CuZr, in particular aimed at testing whether the applied potential is able to well describe the steric aspects of the interaction.

[1] A. Inoue, T. Zhang, and T. Masumoto, Mater. Trans., JIM **30**, 965 (1989).
[2] A. Inoue, A. Kato, T. Zhang, S. G. Kim, and T. Masumoto, Mater. Trans., JIM **32**, 609 (1991).
[3] A. Peker and W. L. Johnson, Appl. Phys. Lett. **63**, 2342 (1993).
[4] G. J. Fan, W. Löser, S. Roth, J. Eckert, and L. Schultz, J. Mater. Res. **15**, 1556 (2000).
[5] A. Inoue, W. Zhang, T. Zhang, and K. Kurosaka, Acta Mater. **49**, 2645 (2001).
[6] U. Rößler, Ph.D. thesis, University of Göttingen, 1995.
[7] M. Guerdane and H. Teichler, Phys. Rev. B **65**, 014203 (2001).
[8] Y. H. Jin, K. Lu, Y. D. Gong, and Z. Q. Hu, J. Chem. Phys. **106**, 8830 (1997).
[9] M. Kluge and H. R. Schober, Phys. Rev. B **70**, 224209 (2004).
[10] H. Teichler, Phys. Rev. E **53**, R4287 (1996).
[11] A. B. Mutiara and H. Teichler, Phys. Rev. E **64**, 046133 (2001).
[12] S. C. Glotzer, J. Non-Cryst. Solids **274**, 342 (2000).
[13] H. Teichler, Phys. Rev. E **71**, 031505 (2005).
[14] J. Horbach and W. Kob, Phys. Rev. B **60**, 3169 (1999).
[15] L. J. Lewis and G. Wahnström, Phys. Rev. E **50**, 3865 (1994).
[16] A. Baumketner, and J.-E. Shea, Y. Hiwatari, Phys. Rev. E **67**, 011912 (2003).
[17] D. Caprion and H. R. Schober, Phys. Rev. B **62**, 3709 (2000).
[18] U. Bengtzelius, W. Götze, and A. Sjölander, J. Phys. C **17**, 5915 (1984).
[19] E. Leutheusser, Phys. Rev. A **29**, 2765 (1984).
[20] W. Götze and L. Sjögren, Rep. Prog. Phys. **55**, 241 (1992).
[21] S. P. Das and G. F. Mazenko, Phys. Rev. A **34**, 2265 (1986).
[22] K. Kawasaki, Physica A **208**, 35 (1994).
[23] W. Kob and H. C. Andersen, Phys. Rev. Lett. **73**, 1376 (1994).
[24] W. Kob and H. C. Andersen, Phys. Rev. E **52**, 4134 (1995).
[25] W. Götze and M. Lücke, Phys. Rev. B **13**, 3825 (1976).
[26] J. L. Barrat and A. Latz, J. Phys.: Condens. Matter **2**, 4289 (1990).
[27] M. Nauroth and W. Kob, Phys. Rev. E **55**, 657 (1997).
[28] W. Götze and R. Hausmann, Z. Phys. B: Condens. Matter **72**, 403 (1988).
[29] H. J. C. Berendsen, J. P. M. Postma, W. F. van Gunsteren, A. DiNola, and J. R. Haak, J. Chem. Phys. **81**, 3684 (1984).
[30] M. W. Finnis, J. Phys. F: Met. Phys. **4**, 1645 (1974).
[31] C. Hausleitner and J. Hafner, Phys. Rev. B **45**, 115 (1992).
[32] C. Hausleitner and J. Hafner, Phys. Rev. B **45**, 128 (1992).
[33] N. Mattern, J. Sakowski, A. Concustell, P. Jovari, M. D. Baro, and J. Eckert (unpublished).
[34] W. Götze and L. Sjögren, Transp. Theory Stat. Phys. **24**, 801 (1995).
[35] H. Vogel, Phys. Z. **22**, 645 (1921).
[36] G. S. Fulcher, J. Am. Ceram. Soc. **8**, 339 (1925).
[37] G. Tammann and G. Hesse, Z. Anorg. Allg. Chem. **156**, 245 (1926).
[38] M. Fuchs, J. Non-Cryst. Solids **172-174**, 241 (1994).

[39] W. Götze and L. Sjögren, J. Phys. C **20**, 879 (1987).
[40] W. Götze and L. Sjögren, J. Phys. C **21**, 3407 (1988).
[41] H. Teichler, Phys. Rev. Lett. **76**, 62 (1996).
[42] G. Wilde, G. P. Görrler, and R. Willnecker, Appl. Phys. Lett. **68**, 2953 (1996).
[43] R. Busch, Z. J. Kim, and W. L. Johnson, J. Appl. Phys. **77**, 4039 (1995).
[44] F. Faupel *et al.*, Rev. Mod. Phys. **75**, 237 (2003).
[45] H. Teichler, Defect Diffus. Forum **143-147**, 717 (1997).
[46] E. Rössler, A. P. Sokolov, A. Kisliuk, and D. Quitmann, Phys. Rev. B **49**, 14967 (1994).